Comprehensive Study to Design Advanced Metal-carbide@Garaphene and Metal-carbide@FeO_x Nanoparticles with Tunable Structure by the Laser Ablation in liquid

Fatemeh Davodi [1], Elisabeth Mühlhausen [2], Daniel Settipani [1], Eeva-Leena Rautama [1], Ari-Pekka Honkanen [3], Simo Huotari [3], Galina Marzun [2], Pekka Taskinen [4], Tanja Kallio *[1]

[1] F. Davodi, D. Settipani, Dr. E. Rautama, Prof. T. Kallio
Electrochemical Energy Conversion Group, Department of Chemistry and Materials Science, School of Chemical Engineering, Aalto University, P.O. Box 16100, FI-00076 Aalto, Finland
Email: fatemeh.davodi@aalto.fi, tanja.kallio@aalto.fi

[2] E. Mühlhausen, Dr. G. Marzun
University of Duisburg-Essen, Technical Chemistry and Center for Nanointegration Duisburg-Essen (CENIDE), Universitätsstr. 7, 45141 Essen, Germany

[3] Prof. S. Huotari, A. Honkanen
Department of Physics, University of Helsinki PO Box 64, FI–00014 Helsinki, Finland

[4] Prof. P. Taskinen
Department of Chemical and Metallurgical Engineering, School of Chemical Engineering, Aalto University, P.O. Box 16100, FI-00076 Aalto, Finland

Graphical Abstract

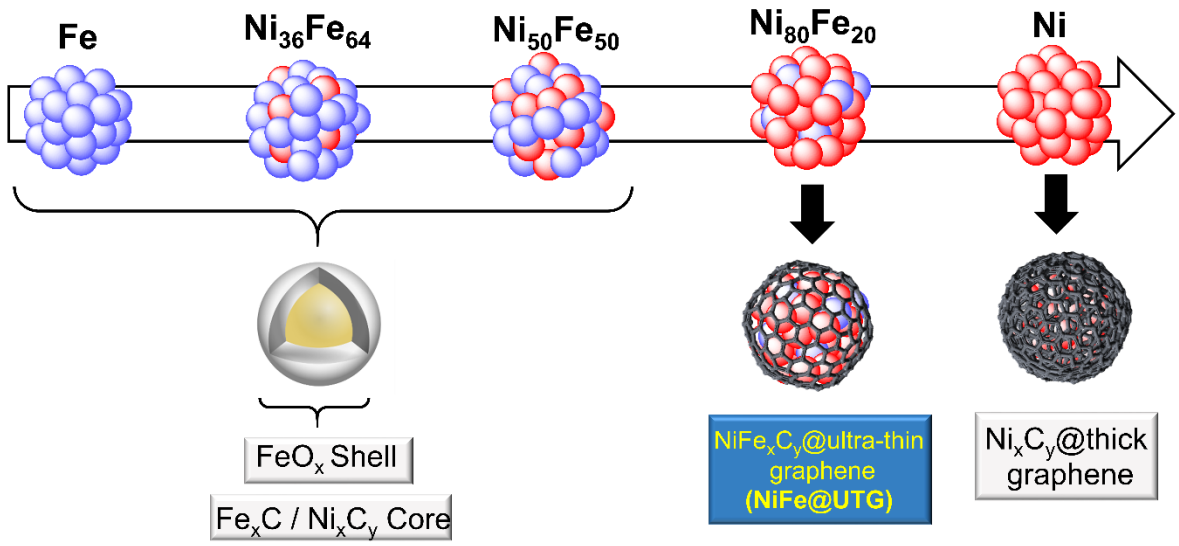

Abstract

Core-shell nanoparticles represent a class of materials that exhibit a variety of properties. By rationally tuning the cores and the shells in such nanoparticles (NPs), a range of materials with tailorable properties can be produced which are of interest for a wide variety of applications. Herein, experimental and theoretical approaches have been combined to show the structural transformation of NPs resulting to the formation of either $NiFe_xC_y$ encapsulated in ultra-thin graphene layer (NiFe@UTG) or $Ni_3C/Fe_xC_y@FeO_x$ NPs with the universal one-step pulse laser ablation in liquid (PLAL) method. Analysis suggests that carbon in Ni_3C is the source for the carbon shell formation, whereas the final carbon-shell thickness in the NPs originates from the difference between Ni_3C and Fe_xC_y phases stability at room temperature. The ternary Ni-Fe-C phase diagram calculations reveal the competition between carbon solubility in the studied metals (Ni and Fe) and their tendency toward oxidation as the key properties to produce controlled core-shell NP materials. As an application example, the electrocatalytic hydrogen evolution current on the different NPs is measured. The electrochemical analysis of the NPs reveals that NiFe@UTG has the best performance amongst the NPs in this study in both alkaline and acidic media.

Keywords: Core-shell nanoparticles, Carbon-shell formation, Metal-carbide, Pulse laser ablation in liquid, Nickel-iron-carbon ternary phase diagram, Hydrogen evolution reaction.

1 Introduction

One focus in nanotechnology is to combine materials properties to generate nanomaterials with new multifunctional properties. This can be achieved, for example, by combining two or more metal components into an alloy or core-shell structures.[1,2] Recently, 3d transition metals and their alloys encapsulated in carbon-based materials (metalcarbide@C) have emerged as promising candidates for different applications such as energy storage [3–8] The fundamental basis of this strategy relies on the electronic modification of graphitic shell by a metallic core. Another prominent advantage of this strategy relies on providing a protective graphitic shell for the core, which significantly improves the durability of the NPs in harsh conditions.[9,10] Since electron transfer and adsorption of the reacting species is affected by the work function of the metallic core and the thickness of the shell, it is predicted that the feasibility of such materials for any applications can be optimized by tuning the physicochemical properties of the metallic core and the number of graphitic layers. Thus, the optimization of these unique materials through structural and electronic modulation enables the most advantageous promotion of the usage of such materials.

Recent density functional theory (DFT) calculations [6,11,12] have shown that charge transfer occurs from the metal cores most efficiently to a single layer carbon shell. These studies demonstrate that the number of graphene layers exhibits a significant impact on the electronic structure of the metal@C nanostructures. However, in experimental studies, the prepared metal@C nanoparticles (NPs) entail a range of carbon shell thicknesses; yet it is technically challenging to make a thin

carbon layer on metal NPs surface. This suggests that effective synthetic protocols should be developed so that these theoretical insights can be directly compared with the experimental data and more importantly, to unravel the origin of the mechanism.

Here we show that by controlling NPs synthesis parameters during pulsed laser ablation in liquid (PLAL) method, an optimal and reproducible metal-carbide@graphene structure can be achieved. In this context, nickel-iron nanoalloys through a one-step and facile PLAL method are encapsulated in ultrathin graphene spheres (NiFe@UTG) and further examined as electrocatalysts for the hydrogen evolution reaction (HER) in both acidic and alkaline media. This study provides a detailed description of the geometric and electronic structure of all samples using different structural analysis and theoretical considerations.

2 Results and discussion

2.1 Synthesis and characterization

2.1.1 NiFe alloy NPs encapsulated in the ultra-thin graphene layer

The NiFe@UTG was synthesized via the PLAL method describes in our previous study [13]. Briefly, nickel-iron alloy NPs encapsulated in an ultra-thin graphene shell (NiFe@UTG) were obtained from a laser ablation process of a $Ni_{80}Fe_{20}$ alloy target picosecond laser (ps-laser) in acetone. Fig. S1 represents the synthesis procedure and economical aspects are briefly discussed in Supporting Information

High-resolution transmission electron microscopy (HRTEM; Fig. 1) images show that the NiFe@UTG samples consist of bimetallic metal nanoparticles (NPs) that are

completely encapsulated by graphene shells. The NiFe@UTG NPs have the average size distribution of 12.5 nm (see the statistical analysis in Fig. S2). Energy-dispersive X-ray (EDX) maps on the single-particle show that Ni and Fe atoms are distributed homogeneously (Fig. 1c), which is also supported by the line scan shown in Fig. S3. Both imaging methods suggest the presence of an alloy structure in the NiFe NPs. In addition, inductively coupled plasma optical emission spectroscopy (ICP-OES) shows the mass ratio of $Ni_{80}Fe_{20}$ for the NiFe@UTG sample (Fig. S3). According to the statistical analysis of almost 100 NPs by HRTEM (Fig. 1c), the graphene shells on the NiFe NPs are very thin, and most of the graphene shells (>90%) consist of only one or two layers.

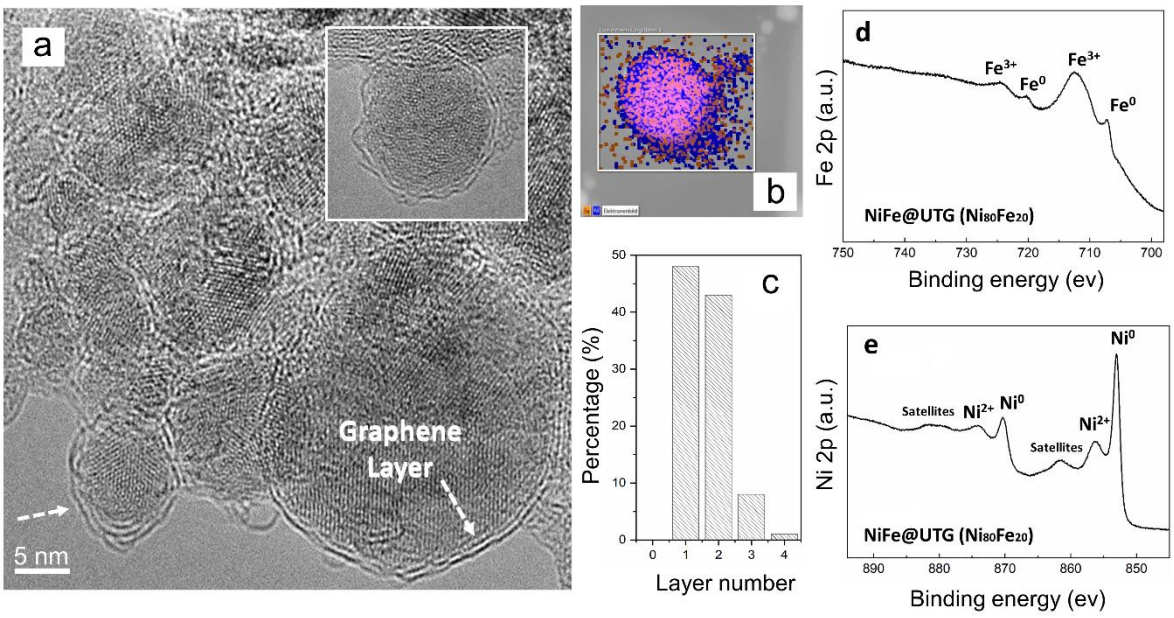

Fig. 1 (a) HRTEM images of NiFe@UTG ($Ni_{80}Fe_{20}$), showing the graphene shell and encapsulated metal nanoparticles with different sizes. The inset indicates the full encapsulation of an individual nanoparticle (arrows demonstrate the graphene layer). **(b)** EDX maps for NiFe@UTG for Ni (blue), Fe (brown) and pink color indicates regions where both Ni and Fe are detected. **(c)** Statistical analysis

of the number of layers in the graphene shells encapsulating the metal nanoparticles in NiFe@UTG. XPS spectrum of NiFe@UTG. **(d)** High-resolution Fe 2p spectrum. **(e)** Ni 2p spectrum.

Chemical states of the NiFe@UTG ($Ni_{80}Fe_{20}$) NPs were measured by X-ray photoelectron spectroscopy (XPS), Fig. S4. In the high-resolution C1s the peaks to sp^2 -hybridization (C-C bond, ~284.5 eV) is observed, and the sample produced a small peak corresponding to carboxylates (O-C=O) at 288.5 eV (Figure S4a). In the Ni 2p and Fe 2p spectra, clear peaks at 707 eV and 853 eV related to metallic Fe and Ni in Fig. 1d and 1e, respectively, suggest that both Fe and Ni maintain their metallic state. Furthermore, oxidized Ni and Fe species are also detected at 855.6 eV and 710.5 eV, respectively, and these are attributed to major carbide and parasite oxide phase as discussed below in the context of the XRD, Raman and XAS measurements. This indicates that NiFe NPs are entirely encapsulated within the graphene shell, which prevents the further oxidation of the metallic phase in NPs when exposed to air and oxidizing environmental.

Generally in PLAL, the interaction of the laser-formed NiFe clusters with oxidizing medium induces the formation of mixed metal oxide and metallic NPs.[13] Reactive oxygen species can be formed in the plasma during laser ablation, and this reactive species can oxidize the particles.[14,15] In this study, the ablation is carried out in acetone, which has a high amount of bonded oxygen (C:O ratio 3:1) as well as dissolved oxygen (solubility of oxygen in acetone 45cm^3/L).[16] Thus the presence of $Fe^{2+/3+}$ species (Fig.1d) and Ni^{2+} (Fig. 1e) can be related to the interaction of iron and nickel with carbon or oxygen and further analysis are needed to find out the structure. The latter can originate from residually dissolved atmospheric or bonded oxygen in acetone or oxygen from H_2O impurities.[15,17] Carbon is from solvent decomposition as discussed below. In any case, these XPS results are consistent

with previous observations of metal cluster formation during the PLAL process.[18,19]

2.1.2 The intrinsic role of laser parameters, solvent and metal-core compositions in the formation of ultra-thin graphene shell in metal@C NPs produced via PLAL

In order to use PLAL as an universal and efficient method for substituting precious metal electrocatalysts with non-precious metal@C structures in energy applications, it is essential to elucidate the role of each compound during the synthesis procedure. Due to the chemical reactions between the metal vapour and the liquid surroundings during the NPs formation process, different oxidation or carbonization states can be achieved by PLAL.[20,21] Hence, by choosing the correct synthesis parameters, PLAL can be a promising method that enables the generation of a variety of nanomaterials for specific applications.

2.1.2.1 Role of laser parameters and solvent on the formation of ultra-thin graphene shells

To illuminate the possible influence of the laser pulse duration on the structure of the final NPs and graphitic carbon thickness, $Ni_{80}Fe_{20}$ alloy was also ablated in acetone solution with a nanosecond laser (ns-laser). Fig. 2 shows the comparison between $Ni_{80}Fe_{20}$ produced with a picosecond laser (ps-laser) and that of produced with the ns-laser. As Fig. 2b reveals NPs created with ns-laser are encapsulated in a thick layer of graphene compared to that of ps-laser ablation, where only a thin graphitic layer is formed (NiFe@UTG NPs). This behaviour is probably due to the pulse

duration that influences the electron cooling time and, consequently, on the heat effect on the surface of the metal target as well as surrounding liquid.[22] Due to the shorter pulses in case of the ps-laser ablation, thermal ablation processes, such as the solvent decomposition, are less likely compared to ablation processes with ns-pulses. Therefore, the slower cooling rate of ns-pulses affects the formation of a thicker graphite shell.

To further explore the full potential of PLAL in producing metal@C NPs, the role of the solvent structure on the thickness of the graphene shell in the NPs was also investigated by using toluene and ethanol instead of acetone. Furthermore, water was used to reveal the dependency of the NPs structure on an inorganic solvent (Fig. 2e). These liquids have been chosen due to their different macroscopic liquid properties and their common use within the PLAL community. Pronounced NiFe encapsulated in carbon shell (NiFe@C) structures are observed in all the studied organic solvents. However, the structure and morphology of the NPs clearly differ. Fig. 2 c-e shows HRTEM images of NPs synthesized in toluene, ethanol and water.

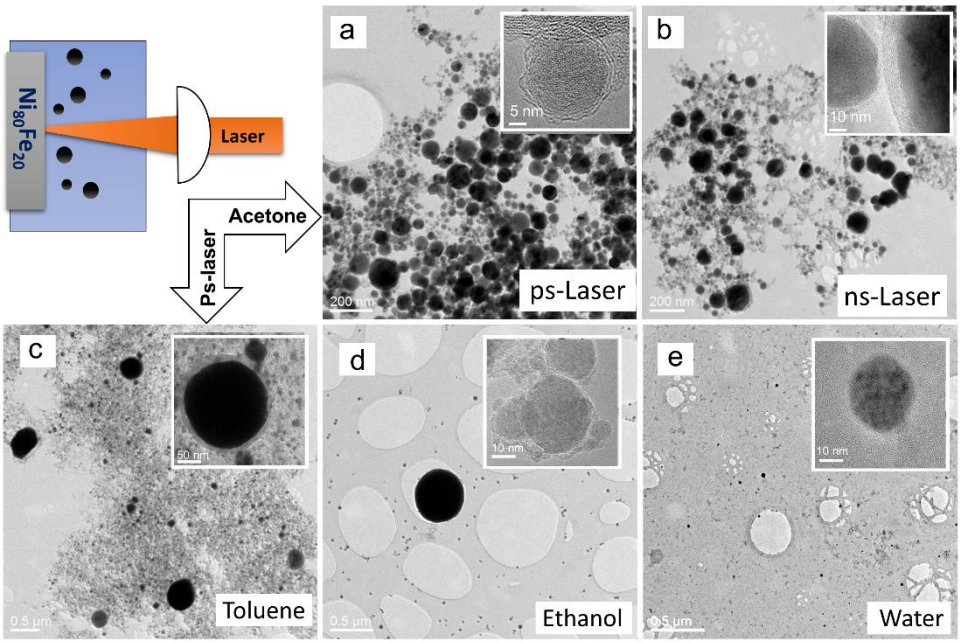

Fig. 2 HRTEM images of NPs produced from $Ni_{80}Fe_{20}$ **(a)** with ps-laser in acetone and **(b)** with ns-laser in acetone, as well as **(c-e)** with ps-laser in toluene, ethanol and water, from left to right.

When working with organic solvents, their degradation is expected during PLAL.[15,23,24] Thus, it is expected that a carbon-shell formation is favoured over solvent integration within the particles. In the case of toluene, irradiating the solvent itself already leads to the formation of a graphene matrix [25], which can also be observed in the presence of nanoparticles.[26] This is due to the significant amount of carbon atoms present within the toluene molecule, resulting in their release by solvent pyrolysis during the ablation process. Based on the amount of carbon atoms within the solvents it is expected that the carbon shell formed on the NPs will be thicker for acetone than for ethanol. However, as can be seen in Fig. 2 a and d, this is not clearly observable. This deviation from the expectation can partly be ascribed to the different NP sizes obtained and thus, to different shell thickness to core size ratios. From literature it is known that the choice of solvent used during PLAL has a significant influence on the particle size distribution [27,28]. Additionally, the solvents

exhibit different chemical activities with the target atoms, both depending on the choice of solvent and target, resulting in different carbon shell thicknesses and different amounts of integrated carbides [29,30]. In the case of NPs produced in water, having a low contrast at the TEM image indicates oxidized nanoparticles as already previously observed [31,32] for Ni and Fe NPs in aqueous solution.

2.1.2.2 The critical role of metal-core composition on the formation of ultra-thin graphene shells

To understand the role of the metal core in the formation an ultra-thin graphene shell in metal@C materials, laser ablation was conducted for a set of metal compositions Ni, $Ni_{80}Fe_{20}$, $Ni_{50}Fe_{50}$, $Ni_{36}Fe_{64}$ and Fe in acetone (see Section 2.1.2.1 for selection of laser parameters and proper solvents). EDX revealed that the atomic compositions of NPs are close to that of the target materials (Fig. S5). Interestingly, NPs show pronounced structural differences and size with the different elemental compositions (Fig. S5-S7 and Table 2). According to HRTEM images, NPs produced from Fe foil have a pronounced Fe@FeO_x structure. Preferential oxidation of Fe in NiFe is described in literature both for bulk and NiFe NPs [33,34]. In very recent work [35], the influence of different metals during laser ablation in acetone has been studied. It has been found that in the case of more inert noble metals, such as Pt, Au and Pd, mainly elemental NPs are obtained. In contrast, some non-noble metals, such as Ti, Mo and Ni, form metal carbide cores whereas other, such as Mn or Fe, tend to form mixtures of metal and metal oxides. In the same work, the tendency to form carbides has been explained by d-orbital-vacancies and subsequently higher binding energy of carbon to the d orbital. The formation of oxides and the

carbonization takes place in the gas phase (cavitation bubble), while the creation of a graphitic shell has been hypothesized to happen in the liquid phase triggered by laser-irradiation metal-catalyzed graphitization. Similar observation is also done in the present work. It has also been shown by DFT calculation that the intermetallic Ni_3Fe is a stable phase in the standard Fe–Ni diagram, while Fe segregation at the surface of the Fe-rich NiFe alloys is expected.[36] Therefore, certain segregation can be expected to occur for Fe-rich alloy compositions. In the next section (2.2), different characterizations and phase diagram calculations have been carried out to further elucidate the possible origin of the phase segregations and structural differences in the NPs.

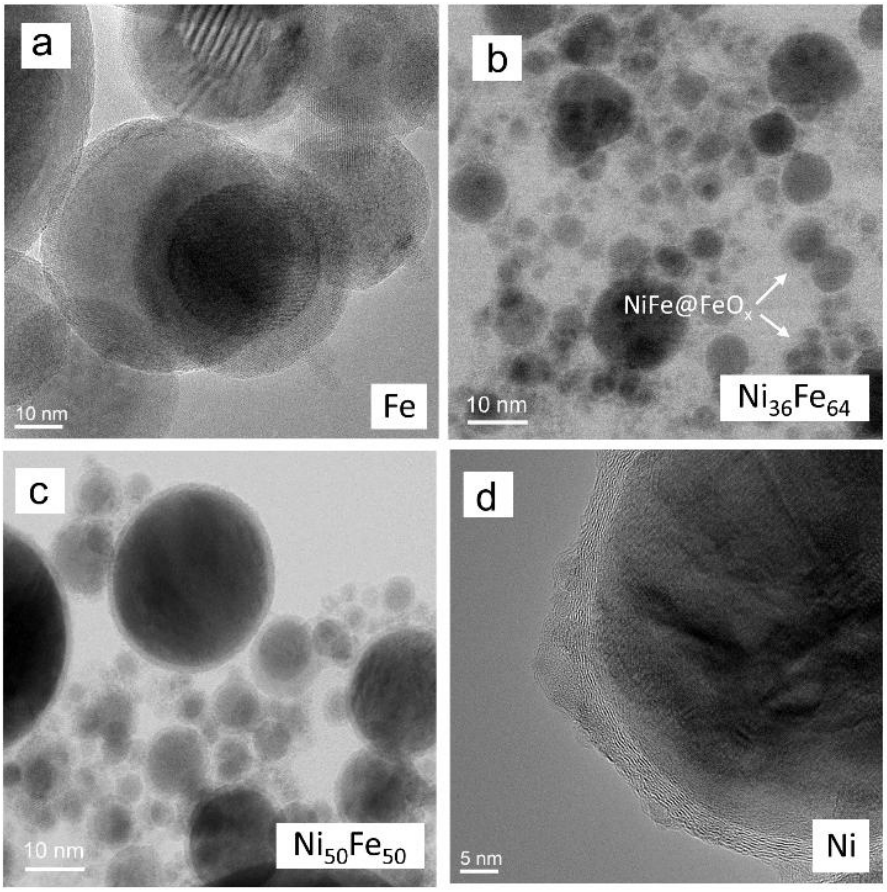

Fig. 3 HRTEM images of NPs synthesized from **(a)** Fe, **(b)** $Ni_{34}Fe_{64}$, **(c)** $Ni_{50}Fe_{50}$ and **(d)** Ni foils with a ps-laser in acetone.

2.2 Structural characterization of NPs produce in acetone with ps-laser

In this section, four precise and detailed structural NP analyses have been performed to clarify the origin of the different structures within the NPs independence of the metal core compositions. Finding the source of elemental segregation is the key parameter, which leads to the formation of NPs with different core-shell structures (Fig. 3).

2.2.1 XRD and RAMAN characterizations

It is expected that metal carbides play an important role in the formation of the graphene-shell around the NPs.[35,37] To elucidate the existence and the type of carbides in the samples, their phase compositions were studied by X-ray diffraction (XRD). The analysis was carried out using information from the International Center for Diffraction Data (ICDD) database and simulations using the program FullProf.[38]

First, the XRD patterns (Fig. 4a and S8) appear similar for all the samples, despite their nominal composition. A closer look reveals the major differences existing and the changes occurring along with the varying Ni-Fe ratio, as explained in more detailed below. The end members, Ni and Fe NPs, were analysed to understand the phase evolution within the series and to identify the carbides and other main phases.

$Ni_{50}Fe_{50}$ and $Ni_{36}Fe_{64}$ samples have very similar phase composition (Fig. S8), and therefore, only the former is included in the main manuscript (Fig. 4a). The Ni sample turns out to be a mixture of two different forms of Ni carbides; a hexagonal (rhombohedric) phase, noted as *h*-Ni_3C, and a cubic phase, *c*-Ni_3C (Fig. 4a, bottom). The same phase composition for Ni NPs has been reported in a previous study [39], in which the cubic phase is reported to be an intermediate carbide phase in the formation of the more typical *h*-Ni_3C. No hexagonal or cubic metallic Ni is present based on their lattice mismatch. When Fe is introduced to the system ($Ni_{80}Fe_{20,}$ $Ni_{50}Fe_{50}$), the main components change to the well-known cubic alloy, Ni_xFe_y [40], *h*-Ni_3C ($Ni_{80}Fe_{20}$) and Fe_7C_3 ($Ni_{50}Fe_{50}$). (Note that the lattice parameters of the cubic Fe-Ni cannot be mistaken to *c*-Ni_3C due to the adequately smaller unit cell of the latter). Also a slight shift in the lattice size of the Ni_xFe_y alloy NPs is observe along an increasing amount of Fe as expected. The fitted lattice parameters of the raw data suggest compositions very close to the expected stoichiometry for the alloy phases (e.g. $Ni_{74}Fe_{26}$ for $Ni_{80}Fe_{20}$ (NiFe@UTG) as interpolated from the database values). In addition to the main components, some parasite phases begin to appear, which are best indexed as metal oxides (NiO and Fe_3O_4/γ-Fe_2O_3). The oxides can especially explain some of the minor reflections, but unfortunately, most of their distinct peaks are superimposed with carbides and Ni_xFe_y alloy. Albeit also the Ni/Fe carbides have overlapping main reflections, they can be distinguished from each other from an additional shoulder that appears on the right side of the Fe_7C_3 main peak. This is distinctively seen the first time in the $Ni_{50}Fe_{50}$ sample but not excluded in $Ni_{80}Fe_{20.}$ Therefore, we must assign these samples to contain both the metal carbides. Finally, the Fe sample is composed mainly of the Fe_7C_3 and a Fe phase that has a small amount of dissolved carbon in the iron lattice; the structure of this (Fe, C) phase is

very similar to that of Ni-Fe alloy but differs from the typical α-Fe. Yet few reflections remain unidentified despite our intensive efforts.

As a summary, XRD clearly confirms the presence of metal carbides in significant amounts in the NPs. The presence of oxides is defined with less certainty and to a much lesser extent but still well supported. Moreover, the amount of *h*-Ni_3C appears to decrease along with increasing Fe content in the measurement series, whereas the amount of Fe_xC_y goes to the opposite direction. It is worth mentioning that XPS analysis for the sample under study, $Ni_{80}Fe_{20}$ (NiFe@UTG) also show oxidized metals (Fig. 1 d and e) to which both carbides and oxides can contribute, as also reported previously [41–44].

Raman spectroscopy is also utilized to reveal each surface phase present in NPs with different ratios (Fig.4b). Raman analysis is a well-known method to investigate the graphitic carbon in the materials and often reveals minority phases not detectable by XRD. Fig. 4b shows that Raman spectra for all the NPs comprise the dominant Raman modes of the defect-induced D mode at 1300–1360 cm^{-1} and the graphitic mode (G mode) at around 1600 cm^{-1}. Here, the I_D/I_G is the intensity ratio of the D band to the G band. The peak intensity ratios of I_D/I_G are calculated to be 14.74, 1.63, 2.05, 0.96 and 0.72 for the Fe, $Ni_{36}Fe_{64}$, Ni_5Fe_5, $Ni_{80}Fe_{20}$ (NiFe@UTG) and Ni samples, respectively. These values of I_D/I_G show increase of the graphitic carbon share as a function of increasing Ni ratio in the metal-core. These results are in a good agreement with other characterizations indicating the crucial role of the Ni to Fe ratio in producing an ultra-thin graphene layer.

Raman spectroscopy further supports the presence of Fe-oxides in the NPs. Raman features at the low-frequency region for the NPs prepared with Fe-target (Fig. 3a)

agrees well with hematite structure. [45,46] The $Ni_{50}Fe_{50}$ and $Ni_{36}Fe_{64}$ samples have similar Raman spectra at the low-frequency region (Fig. 4b) that display the most strong peak in this region at ~690 cm^{-1} and two weaker peaks at ~572 and ~461 cm^{-1}. The strongest peak at ~690 cm^{-1} is attributed to maghemite (γ-Fe_2O_3) since only this phase of iron oxide shows its most pronounce Raman peak at this position [47], and for the small-sized maghemite NPs, this is almost the only observable Raman band.[47]

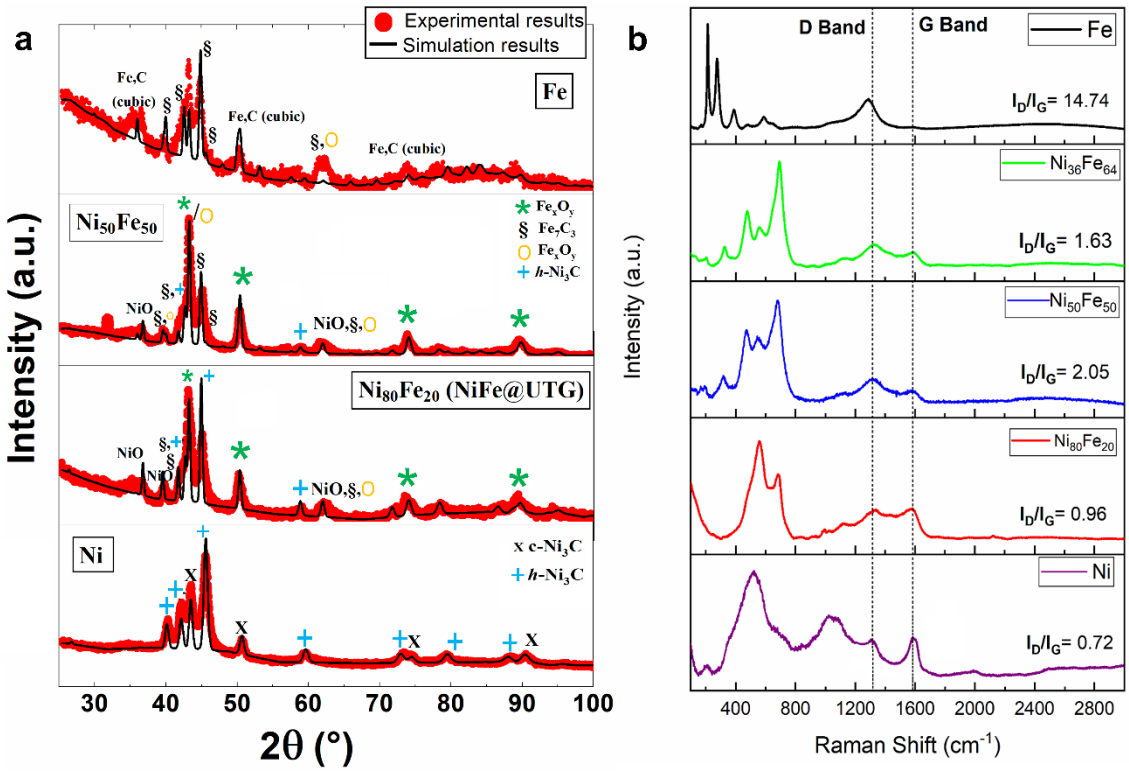

Fig. 4 (a) Measured (red) and simulated (black) XRD patterns with the obtained compositions and **(b)** Raman spectra for Fe, $Ni_{36}Fe_{64}$, $Ni_{50}Fe_{50}$, $Ni_{80}Fe_{20}$ (NiFe@UTG) and Ni.

Based on these XRD and Raman analyses, Fe favors formation of more amorphous carbon layers. Hence, the presence of Ni_3C plays a predominant role in the formation of graphite layers, as also suggested by other studies.[37,48]

2.2.2 X-ray absorption near edge structure (XANES) at the Fe K-edge.

Next, X-ray absorption spectroscopy (XAS) analysis is implemented (Fig. 5 and Fig. 6) to investigate the local structures and chemical states of Fe and Ni in the synthesized NPs. [49] The Fe K-edge normalized XANES spectra of the NPs compared with standards are shown in Fig. 5a and 5c. Fig. 5a inset 2 shows that the absorption edges of the NPs are located in between the metallic reference Fe foil and that of the powder oxidized Fe standards (i.e. Fe_2O_3 and Fe_3O_4). The oxidation states are further investigated by plotting the energy shifts in the half-height of the absorption edge against the formal iron oxidation state of the standard samples (i.e. +0 for Fe foil, +2.67 for Fe_3O_4 and +3 for Fe_2O_3). As a result, a linear function is derived and used to qualitatively asses the average oxidation state of Fe in the NP samples. The results of this estimation are shown in Table S1 and Fig. 5b and suggest that all the samples contain metallic and oxidized Fe. This is well in agreement with XRD observations of the presence of Ni_xFe_y alloy and major Fe carbide and parasitic oxide phases in the bimetallic NPs. Likewise, for the end member monometallic Fe NPs these observed intermediate oxidation states support the XRD and Raman findings of coexistence of metallic Fe and Fe carbides and oxides.

Furthermore, as it can be seen in both Fig. 5a and 5c, inset 1, there is a lack of sharpness in the pre-edge absorption feature of the NPs, which could indicate either metallic iron, iron carbide, or coexistence of both. [50,51] In addition, as seen in the inset 3 in Fig. 5a and 5c, a partial change of the edge crest peaks of the NPs is also observed (i.e. the crest peaks are higher than those in the standard Fe foil and lower than those from the oxides standards), which is another indication of the presence of iron carbide in these samples .[48] On the other hand, the XANES derivative spectra in Fig. 5d confirms the presence of not only metallic iron in the NPs (i.e. Fe^0 in the Fig. 5d) but also other oxidized species such as Fe^{2+} and Fe^{3+}, which further indicates the existence of Fe carbides, nitrides or oxides.[50] For the studied NPs, due to the nature of the synthesis process, the presence of nitrides is discarded. As can be seen from the inset in Fig. 5d, all the NPs have spectral signals with two distinctive peaks at ~ 7112 eV and ~ 7124 eV, related mostly to metallic iron and oxidized species, respectively. In Fig. 5d can also be observed that the Fe NPs have the lower metallic contribution and the highest oxidized contribution of all. On the contrary, in the NiFe alloy NPs, with increasing Ni content, the Fe metallic component increases while the oxidized Fe component decreases. It is worth mentioning that the $Ni_{80}Fe_{20}$ (NiFe@UTG) NPs shows the highest metallic Fe contribution and the lowest oxidized Fe contribution amongst the NiFe NPs.

Taking into consideration the energy position and overall spectral shape of the standard iron carbide (Fe_3C) shown in Fig. 5d, it is difficult to confirm the definitive existence of Fe_3C in the studied NPs. More detailed studies involving the EXAFS region are necessary to verify its presence [35,48,50,51]. However, based on the previously described observations in XANES measurements, and also on the synthesis procedure, the formation of different iron carbide compound is possible.

Hence, phase diagram calculation (Section 2.2.3) has been carried out to give a better insight into the eventual creation of carbides in the samples.

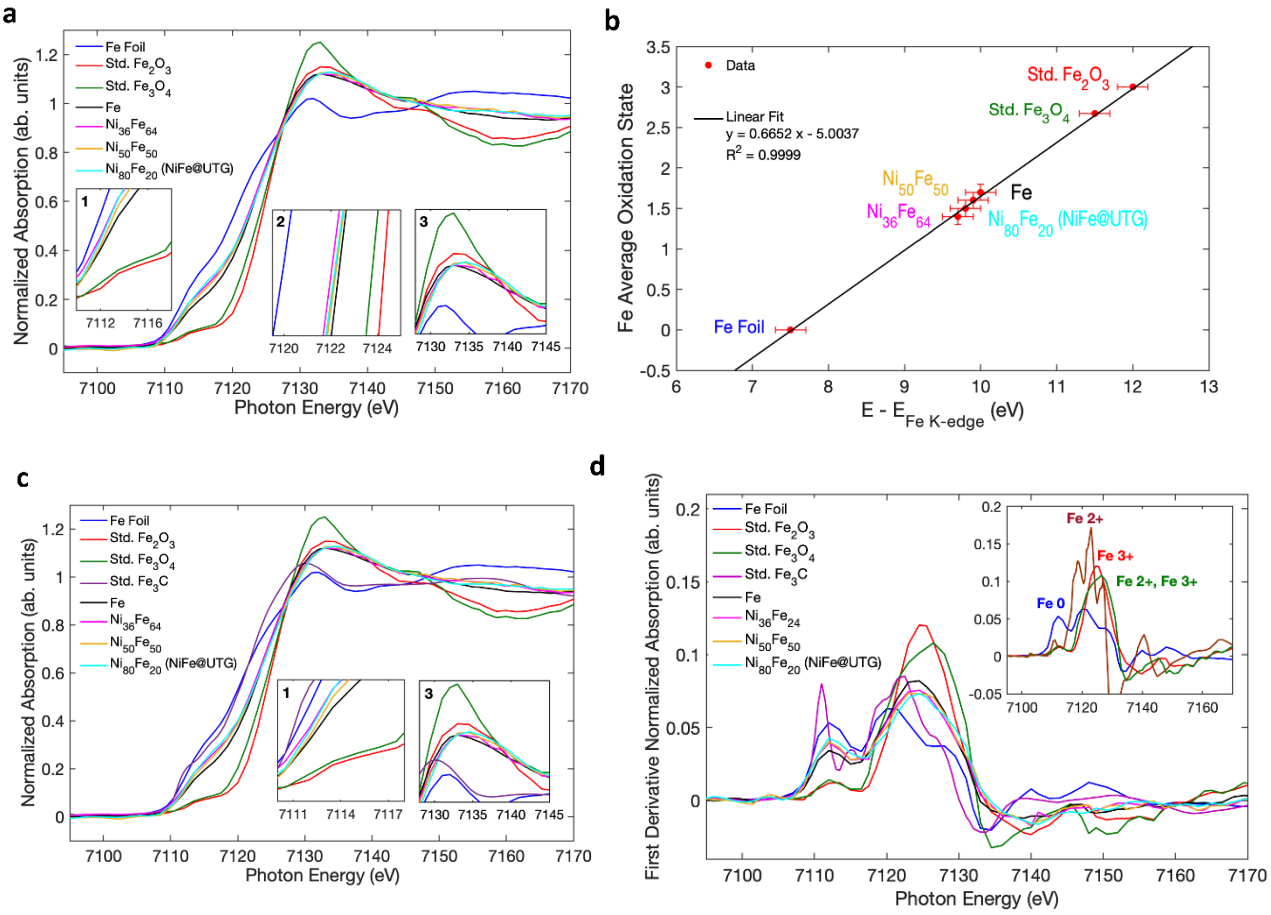

Fig. 5 Normalized XANES spectra at the Fe K-edge of the NPs in comparison to **(a & c)** the bulk oxide powder standards, the Fe foil, and **(c)** the Fe_3C standard. The inset 1, 2 and 3 correspond to an enlarged pre-edge, half-height of the absorption edge, and edge crest maxima regions, respectively. **(b)** The plot of the Fe average oxidation state vs energy shifts in the half-height of the absorption edge in Fig. (a). **(d)** Normalized first derivate XANES spectra of the NPs in comparison to the bulk oxide powder and the Fe_3C standards. The inset shows the normalized first derivative XANES spectra of different Fe species, i.e. Fe^{0} (Fe Foil), Fe^{2+}, Fe^{3+} (Std. Fe_2O_3), and Fe^{2+}, Fe^{3+} (Std. Fe_3O_4).

X-ray absorption near edge structure (XANES) at the Ni K-edge. The Ni K-edge normalized XANES spectra of both the standards and synthesized nanoparticles are shown in Fig. 6a. Unlike the Fe K-edge XANES spectra, in general, the overall spectral shape derived from the NPs are all quite close and similar to that of the Ni foil, which indicates the primary metallic character of Ni in all of the samples. [50] Upon more careful observation of the NPs spectra (Fig. 6a), the NP samples can be differentiated into two groups showing similar absorption features. The first group involves the Ni NPs and $Ni_{80}Fe_{20}$ (NiFe@UTG), whereas the $Ni_{36}Fe_{64}$ and $Ni_{50}Fe_{50}$ NPs comprise the second group. The similarity of the structure of the latter ones is already noted in the context of XRD analysis as discussed above. This association serves as a first indication that indeed, atoms in each sample in these two groups share a similar local structure. This is also observed in the XANES analysis of the Fe K-edge. These results are in good agreement with the HRTEM images (Fig. 3).

According to recently reported results, [52] comparing the position and height of the peaks in the normalized first derivate spectra of the NPs (Fig. 6b) can reveal the presence of Ni_3C. Furthermore, the highest peak appears at ~ 8343 eV for materials containing Ni_3C, while for materials with metallic Ni (i.e. FCC – Ni samples) it

appears at ~ 8333 eV.[52] In this respect, the NPs studied here have the highest peak close to 8343 eV, which indicates the presence of Ni_3C in the NPs. Furthermore, taking into consideration the differences between the peak heights shown in Table 1, there is a correlation between Ni content in the NPs, their peak height difference and their structure. If it is considered that both the Ni and $Ni_{80}Fe_{20}$ (NiFe@UTG) NPs share a similar local structure, it can be concluded that the higher the Ni content, the larger the height difference. Similarly, this behaviour is repeated in the case of the $Ni_{36}Fe_{64}$ and $Ni_{50}Fe_{50}$ NPs, where the latter also exhibit a larger height difference in comparison to the lower Ni content sample (Table 1). It can be concluded that once the NPs share a similar local structure, Ni-rich NPs contain more Ni_3C.

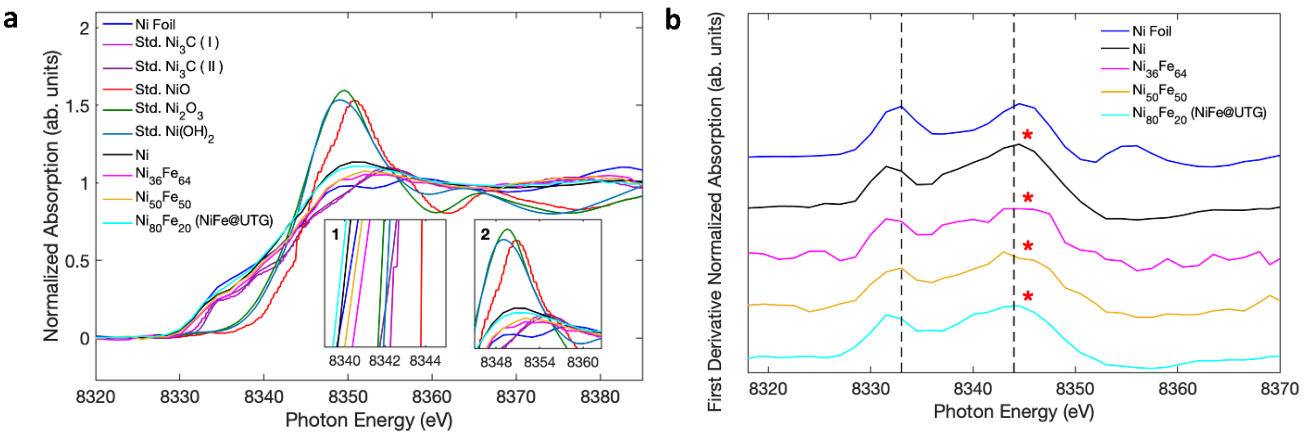

Fig. 6 (a) Normalized XANES spectra at the Ni K-edge of the NP samples in comparison to Ni_3C and Ni oxide standards. The insets 1 and 2 correspond to the half-height of the absorption edge and edge crest maxima regions, respectively. **(b)** Normalized first derivate XANES spectra at the Ni K-edge of the NP samples. The dashed lines mark the energy positions at 8333 eV and 8343 eV respectively. The * marks the peak with the greatest height magnitude for each of the samples. There is no * mark for the Ni foil since the peak difference is too low, i.e. ~ 0.004. The Std. Ni_3C (I), and the NiO standard

are extracted from Ref. [53] The Std. Ni_3C (II), is extracted from the Ref. [54] Ni oxide standards are obtained from the online XAFS Database.[55]

Table 1. Energy positions and heights of the maxima peaks in the normalized first derivate XANES spectra at the Ni K-edge.

First Derivative Peak heights					
Samples	**Energy Position 1ST Max. Peak (eV)**	**Height (ab. units)**	**Energy Position 2nd Max. Peak (eV)**	**Height (ab. units)**	**Height Difference (ab. units)**
Ni Foil (Sta.)	8333	0.0709	8344	0.0746	0.0037
Ni NPs	8332	0.0572	8344	0.0881	0.0309
$Ni_{80}Fe_{20}$ NPs **(NiFe@UTG)**	8332	0.0600	8344	0.0730	0.0130
$Ni_{50}Fe_{50}$ NPs	8333	0.0555	8343	0.0781	0.0226
$Ni_{36}Fe_{64}$ NPs	8332	0.0540	8344	0.0682	0.0142

2.2.3 Ternary and binary phase diagram calculations

The metastable Ni-Fe-C ternary phase diagram at atmospheric pressure and different temperatures from 1500°C up to 500°C is calculated (Fig. 7 a-f) to elucidate the phase segregation in NPs formation during the PLAL synthesis. For a better insight into the ternary phase diagrams of the Ni-Fe-C system, the binary phase diagrams of Fe-C and Ni-C systems (Fig. 8) are also calculated.

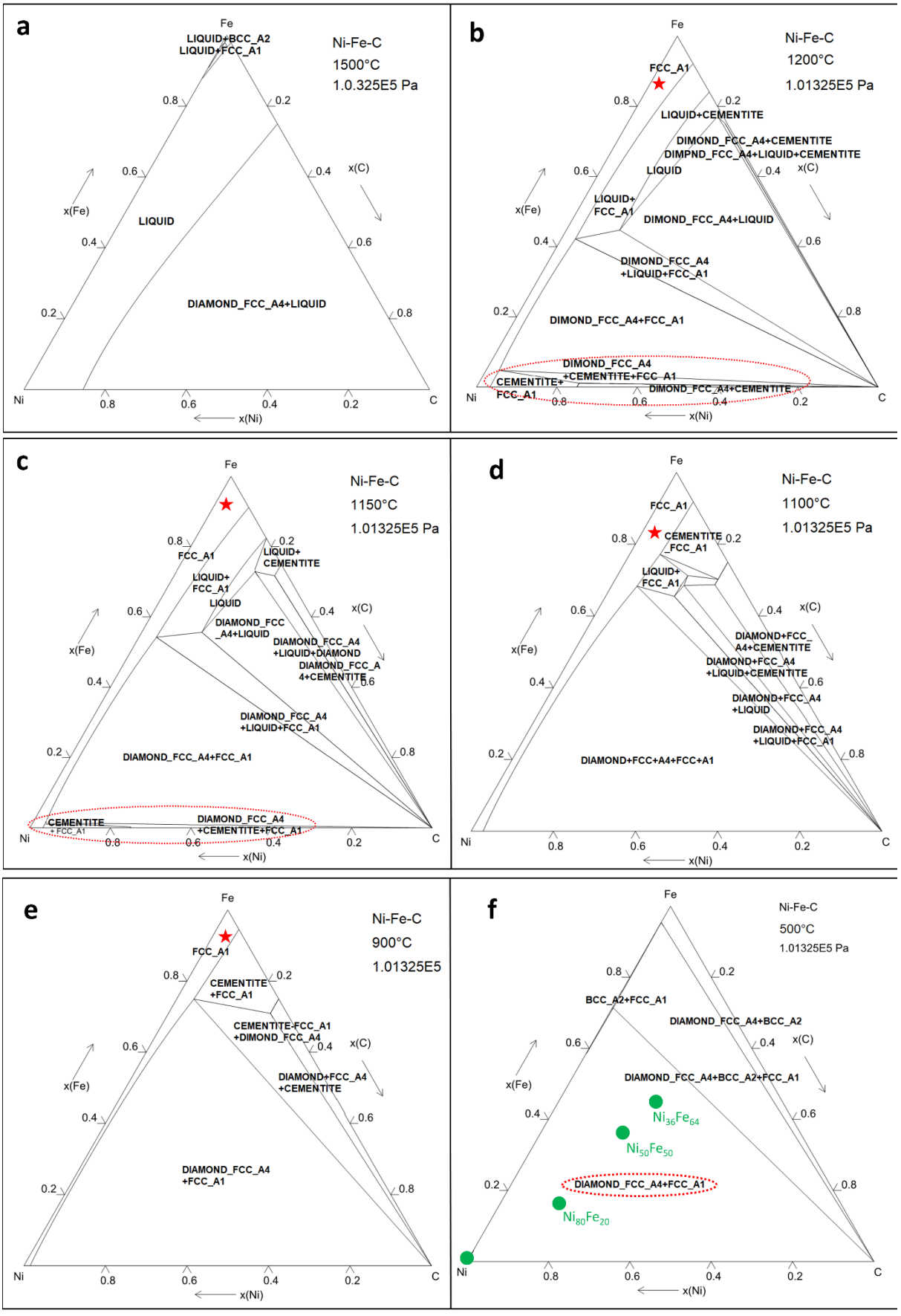
a
Fe
LIQUID+BCC_A2
LIQUID+FCC_A1
Ni-Fe-C
1500°C
1.0.325E5 Pa
LIQUID
DIAMOND_FCC_A4+LIQUID
x(Fe)
x(C)
x(Ni)
Ni
C
b
Fe
FCC_A1
Ni-Fe-C
1200°C
1.01325E5 Pa
LIQUID+CEMENTITE
DIMOND_FCC_A4+CEMENTITE
DIMPND_FCC_A4+LIQUID+CEMENTITE
LIQUID
LIQUID+
FCC_A1
DIMOND_FCC_A4+LIQUID
DIMOND_FCC_A4
+LIQUID+FCC_A1
DIMOND_FCC_A4+FCC_A1
DIMOND_FCC_A4
+CEMENTITE+FCC_A1
CEMENTITE+
FCC_A1
DIMOND_FCC_A4+CEMENTITE
c
Fe
Ni-Fe-C
1150°C
1.01325E5 Pa
FCC_A1
LIQUID+
CEMENTITE
LIQUID+
FCC_A1
LIQUID
DIAMOND_FCC
_A4+LIQUID
DIAMOND_FCC_A4
+LIQUID+DIAMOND
DIAMOND_FCC_A
4+CEMENTITE
DIAMOND_FCC_A4
+LIQUID+FCC_A1
DIAMOND_FCC_A4+FCC_A1
CEMENTITE
+ FCC_A1
DIAMOND_FCC_A4
+CEMENTITE+FCC_A1
d
Fe
Ni-Fe-C
1100°C
1.01325E5 Pa
FCC_A1
CEMENTITE
_FCC_A1
LIQUID+
FCC_A1
DIAMOND+FCC_
A4+CEMENTITE
DIAMOND+FCC_A4
+LIQUID+CEMENTITE
DIAMOND+FCC_A4
+LIQUID
DIAMOND+FCC_A4
+LIQUID+FCC_A1
DIAMOND+FCC+A4+FCC+A1
e
Fe
Ni-Fe-C
900°C
1.01325E5
FCC_A1
CEMENTITE
+FCC_A1
CEMENTITE-FCC_A1
+DIMOND_FCC_A4
DIAMOND+FCC_A4
+CEMENTITE
DIAMOND_FCC_A4
+FCC_A1
f
Fe
Ni-Fe-C
500°C
1.01325E5 Pa
BCC_A2+FCC_A1
DIAMOND_FCC_A4+BCC_A2
DIAMOND_FCC_A4+BCC_A2+FCC_A1
Ni36Fe64
Ni50Fe50
DIAMOND_FCC_A4+FCC_A1
Ni80Fe20

Fig. 7 Metastable ternary phase diagrams of Ni-Fe-C system at atmospheric pressure (in the absence of graphite).

The Fe-C binary subsystem in Fig. 7a shows the formation of cementite (red circle) which is stable from room temperature to the decomposition point (≈1150 °C) while dissolves some Ni and forms a continuous FCC_A1 solution phase. This phase is also shown in the ternary phase diagram at various temperatures, e.g. at 1150 °C, indicating that cementite (Fe_3C) precipitates as primary phase instead of elemental graphite (red circle in Fig. 7b and 7c) forms.

On the other hand, the Ni-C binary subsystem (Fig. 8b) has a similar carbide (red circle), but it does not dissolve iron.[56] This carbide is only stable in a small temperature range in atmospheric pressure and decomposes to diamond-like carbon and metallic Ni (indicated in Fig. 7f).

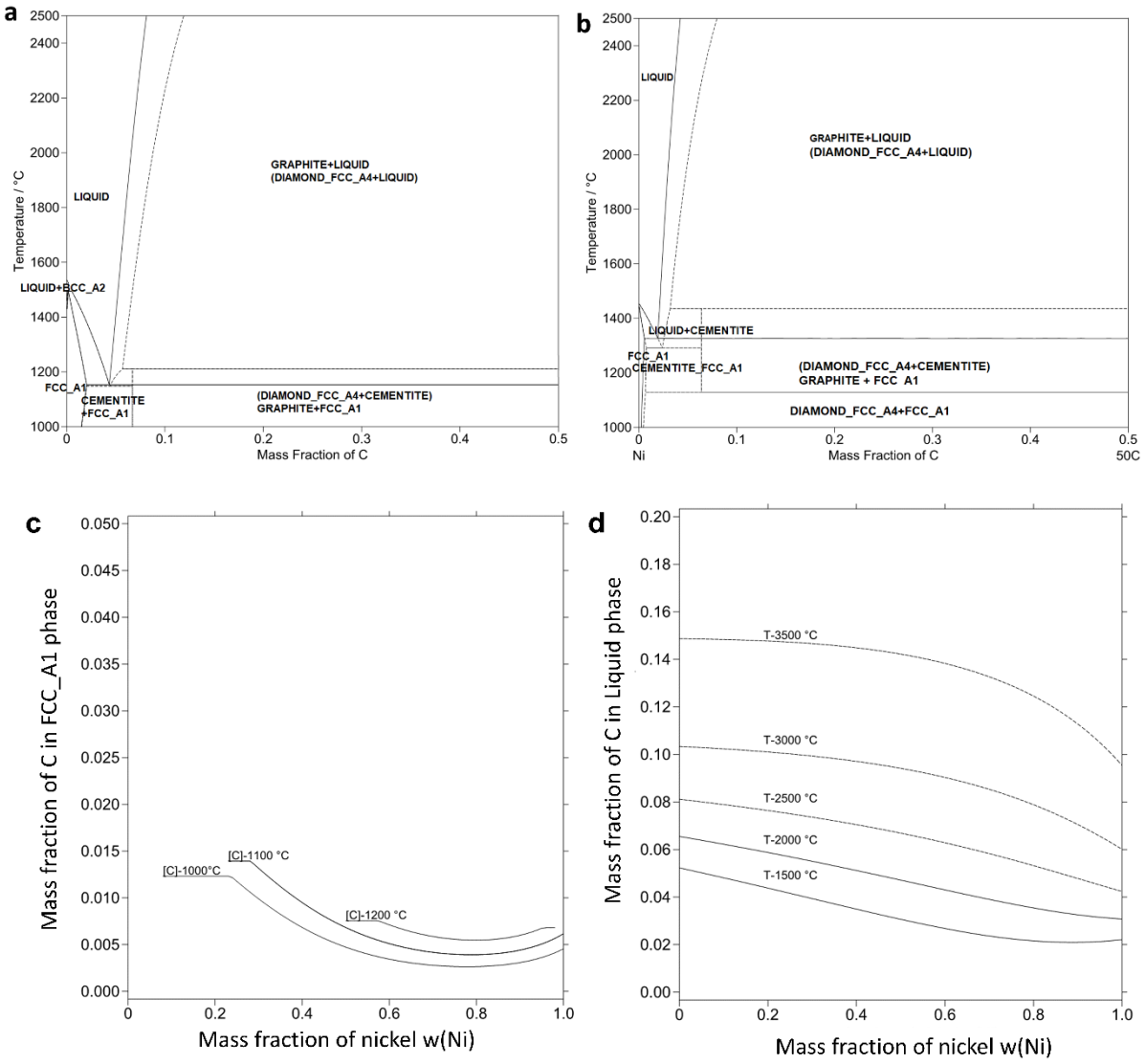

Fig. 8 Binary phase diagram for **(a)** Fe-C system and **(b)** Ni-C system. (— stable phase assemblage; --- metastable assemblage in the absence of graphite). **(c)** Metastable solubility of carbon in solid NiFe alloys (FCC_A1) at 1000-1200 °C in the absence of graphite in the system. **(d)** The solubility of graphite in molten Fe-Ni alloys at 1500-3500 °C.

To further elucidate the origin of the graphitic-shell in the NPs, the solubility of carbon in solid iron-nickel alloys (FCC_A1) and solubility of graphite in the liquid Ni-Fe are also calculated and depicted in Fig. 8c and Fig. 8d, respectively. The upper

temperature for the phase equilibria of condensed NiFe alloys is considered to be around the boiling points of pure Ni and Fe (3000 °C in atmospheric pressure [57]). As it is seen in both Fig. 8c and Fig. 8d, the solubility of pure carbon and graphite in the solid iron-nickel alloys (FCC_A1) and liquid NiFe alloys, respectively, decreases at high temperatures along with increasing Ni concentration in the alloy. Therefore, it is clear that firstly Ni_3C forms and later decomposes to diamond-structured carbon as the primary phase, which is also shown in the Ni-Fe-C ternary phase diagrams (Fig. 7f) and is in a good agreement with previous reports. [35,37]

Based on the observation in phase diagram calculations, a definite conclusion can be made about the possible origin of the ratio-dependent differences of the NP structures (Schematic 1). The ternary phase diagram of Ni-Fe-C system at equilibrium temperature (Fig. 7f) shows that all the NP are in the same phase domain (indicated by green dots) although the above analysis shows indisputable structural differences. This phenomenon can be described as follows: the NPs structures are not stable when they reach room temperature since the cooling rate is rapid during the PLAL synthesis method (10^{10} K/s [58]). It is shown within the Fe-C binary phase diagram (Fig. 8a) that Fe_3C is formed at equilibrium temperature (1150°C) and since the cooling rate of Fe_3C[59] is slow, its structure is preserved at room temperature and does not decompose to Fe and diamond-like carbon (in contrary to Ni_3C). Therefore, in Fe-rich NPs, it is assumed that Fe_xC_y with some dissolved Ni is formed as the core. Moreover, as Fig. 8c shows, by increasing the Ni content, the carbon solubility decreases in the Ni-rich NPs. Therefore, the Fe-rich NPs contain Fe_xC_y precipitates forming instead of carbon exsolution.

On the other hand, as Fe is more reactive toward oxidation than Ni [22,60] in Fe-rich NPs, a FeO_x-shell is observed which is formed later, during the second phase formation (after NPs formation). In Ni-rich samples, more Ni_3C is formed because of higher carbon solubility in Ni. Also, Ni_3C is not stable up to room temperature, as seen in the Ni-C binary phase diagram (Fig. 8b). Thus, during the cooling process, Ni_3C is decomposed to Ni and graphene and some dissolved Fe. This is also observed within the ternary phase diagrams of Ni-Fe-C from high temperature (1200°C) to equilibrium temperature (500°C), where the carbon solubility in the metal alloy phase domain next to the Ni-Fe binary line is reduced to less than 1 at%. Hence, in such conditions in the NPs Fe oxidation and carbon solubility are competing processes[18] and the saturation is not reached leading to the formation of a Fe_xC_y/Ni_3C-core and Fe-oxide shell for Fe-rich samples. Also, the Fe-oxide has a porous structure, compared to other oxides such as NiO_x,[60] and oxygen penetrates it faster, allowing the formation of a thick layer of FeO_x-shell even at low temperatures. Hence, in the case of NiFe@UTG ($Ni_{80}Fe_{20}$), no Fe segregation is expected from the alloy and solubility of carbon is very low, so no oxidation but the formation of the graphene shell is observed. These findings are also observed in the XANES and XRD measurements, as discussed above. Schematic 1 depicts the possible mechanisms and parameters that influence the core-shell NPs formations. Table 2 presents a detailed structural comparison of the NPs with the different Ni/Fe ratios.

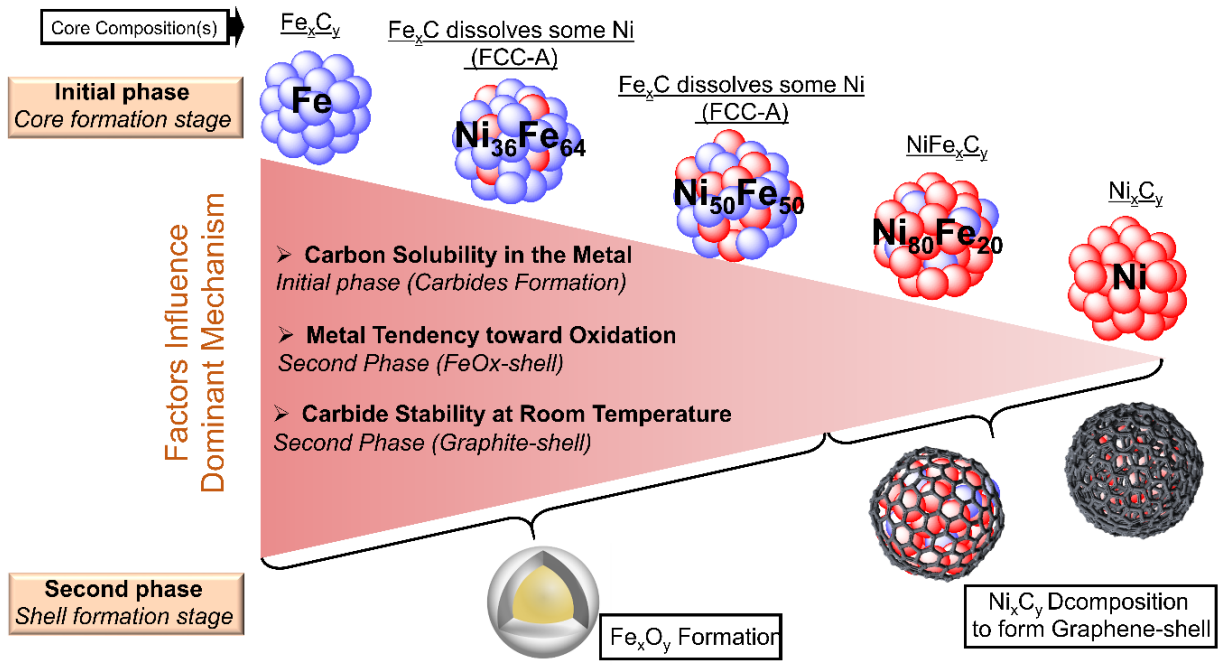

Schematic 1. The proposed thermodynamic mechanism of NiFe@UTG and metal@Fe_xO core-shell nanoparticles formation.

Table 2. The different NPs structure with different metal target composition in acetone with ps-laser.

Metal targets	Core composition (XRD)	Shell composition (Raman)
Ni	Ni	Graphene layer (~10 nm)
Fe	Fe_xC_y	α-Fe_2O_3
$Ni_{36}Fe_{64}$	Ni_3C/Fe_xC_y	γ-Fe_2O_3
$Ni_{50}Fe_{50}$	Ni_3C/Fe_xC_y	γ-Fe_2O_3
$Ni_{80}Fe_{20}$ (NiFe@UTG)	NiFe alloy	Graphene layer (1-3 layers)

3 Electrochemical analysis

To investigate the effect of the different core-shell structures and metal-carbide cores on the NPs' catalytic activity, electrochemical HER tests were performed as an example application. A typical three-electrode setup was adopted to evaluate the HER performance of the synthesized NPs in 0.5 M H_2SO_4 and 0.1M NaOH media. All catalysts were deposited on a glassy carbon electrode with a similar loading of ~0.2 mg cm^{-2} (details in SI). Fig. 9a and 9b show typical polarization curves of the NiFe alloy NPs with different metal ratios and the pure metal NPs in acid and alkaline media, respectively. Among them, NiFe@UTG shows the best catalytic activity toward HER with an onset potential of 110 mV vs RHE and $\eta_{HER,10}$=300 mV within the acid and with an onset potential of 120 mV vs RHE and $\eta_{HER,10}$=400 mV vs RHE within the alkaline. However, the catalytic activity of the NPs produced with different

metal compositions reveals an interesting trend in both the media: Ni <$Ni_{34}Fe_{64}$ <$Ni_{50}Fe_{50}$ <Fe <$Ni_{80}Fe_{20}$ (NiFe@UTG). The electrochemical behaviour of the material in this study is attributed to the unique core-shell structure of the NPs indicating the crucial role of the NP structure that should be taken into account for designing efficient electrocatalysts.

The activity of the metal@C structure is primarily attributed to an interfacial charge transfer from the metal core to the carbon shell that manipulates the electronic interactions between the NP surface and reacting species. Therefore, the activity of such materials varies with the structures and morphologies of the metal core (elemental composition, etc.) and carbon shell (layer thickness, etc.). In this view, the $Ni_{80}Fe_{20}$ and Ni NPs with similar metal@C structures show quite different catalytic activity. Moreover, our results for the NPs with the same metal-core ($Ni_{80}Fe_{20}$) but different carbon-shell thickness (NPs in different organic solutions as well as those synthesized with ns-laser, Fig. S9) further indicate the vital role of carbon shell thickness in the production of an efficient electrocatalyst.

Furthermore, when comparing the HER activity of the $Ni_{50}Fe_{50}$ and Fe NPs in Fig. 9, a clear difference between their current densities is observed. However, the onset potential is the same for both the NPs. This indicates that different cores significantly affect the properties of their metal-oxide (shell) in the core-shell catalyst systems. Based on these results, Fe_xC_y-core enhances more the catalytic activity compared to Ni_3C-core of the FeO_x-shell. Also, the intrinsic properties of oxides in terms of surface morphology and conductivity may play an essential role in the activity in such core-shell NPs. These results show the vital role of the core as a modifier of catalyst properties for enhancing the shell activity.

Tafel plots based on polarization curves in Fig. 9 are acquired to calculate the electrochemical kinetic parameters of Tafel slope for commercial Pt/C and NiFe@UTG ($Ni_{80}Fe_{20}$), as shown in Fig. S10. The difference Tafel slopes suggest that the HER mechanism differs for Pt/C reference and the core-shell NPs. The Tafel slope of 48 mV/decade for NiFe@UTG in acidic media compared to Tafel slopes of 32 mV/decade for Pt/C showed that this material catalyzes the HER through a Volmer–Heyrovsky mechanism [7,61–63].

As for the durability, in the case of NiFe@UTG, almost similar electrochemical behaviour can be observed after 1,000 HER cycles (Fig. S11). This indicates that the NPs are fully encapsulated within the graphitic carbon layers leading to their high durability/stability. To further show the structural stability of the NPs, HRTEM images were taken after durability measurements (Fig. S12), which show NPs preserving their structure even after the long-term measurement.

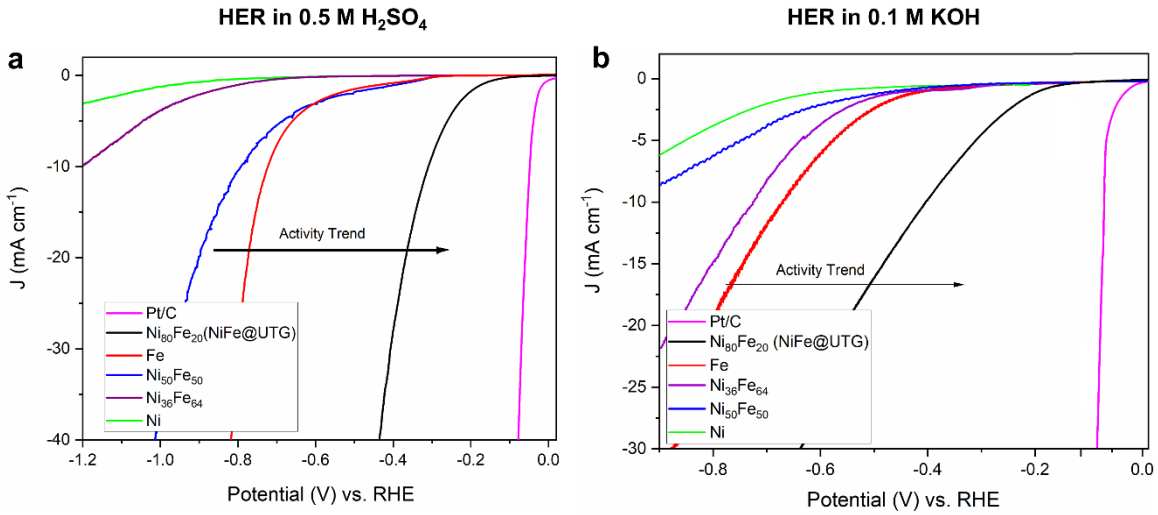

Fig. 9 HER polarization curves of Fe, $Ni_{36}Fe_{64}$, $Ni_{50}Fe_{50}$, $Ni_{80}Fe_{20}$ (NiFe@UTG) and Ni samples (produced in acetone with ps-laser) in comparision to commercial Pt/C catalyst analyzed in **(a)** 0.5 M H_2SO_4 and **(b)** in 0.1 M KOH. All measurements carried out at a scan rate of 10 mV s^{-1}.

4 Conclusion

In summary, we have developed a facile and universal protocol to synthesize ultra-thin graphene encapsulated 3d transition metals, such as Fe, Ni and their alloys with a tunable structure via one step PLAL. Our results indicate that the metal-core composition, the choice of solvent for the ablation process and the laser pulse duration have vital effects on the final NP structure and more importantly on the graphene shell thickness and thus on their corresponding catalytic activities. Ternary phase diagram calculations for the Ni-Fe-C system and XANES results for a set of metal compositions (Ni, $Ni_{80}Fe_{20}$, $Ni_{50}Fe_{50}$, $Ni_{36}Fe_{64}$ and Fe) suggested that the $Ni_{80}Fe_{20}$ alloy is the most promising candidate in terms of the metal ratio between Ni and Fe to construct metal NPs encapsulated within an ultra-thin graphene layer. This is attributed to $Ni_{80}Fe_{20}$ ability to offer a proper balance between carbon solubility and metal oxidation during the synthesis procedure. This level of structural details provides unprecedented insight into the phases present in the carbon-containing core-shell NPs and their evolution. This work serves as a benchmark for the characterization of core-shell NPs by the abovementioned characterization methods. This study provides a universal insight into the field of efficient carbide NP synthesis

also for other transferable synthesis methods, such as arc discharge, spark, chemical vapour depositions (CVD) and metal-organic framework (MOFs).

Acknowledgements

This work is supported by Academy of Finland (the DEMEC 13286266, SUPER 292554 and CloseLoop 13303452 projects) and by the German Federal Ministry of Education and Research (BMBF) within the project NEMEZU (03SF0497C). This work made use of the Aalto University Nanomicroscopy Center (Aalto-NMC) and RaMI Raw material Infrastructure premises. Thanks to Florian de Kock, Merlin Schmuck, Dr Jani Sainio and Dr Hua Jiang for XRD, XPS and HRTEM measurements, respectively. Also, thanks to Dr Bilal Gökce for supervising work at the University of Duisburg-Essen.

References:

[1] R. Ferrando, J. Jellinek, R.L. Johnston, Nanoalloys: From theory to applications of alloy clusters and nanoparticles, Chem. Rev. 108 (2008) 845–910. doi:10.1021/cr040090g.

[2] A.L. Strickler, M. Escudero-Escribano, T.F. Jaramillo, Core-Shell Au@Metal-Oxide Nanoparticle Electrocatalysts for Enhanced Oxygen Evolution, Nano

Lett. 17 (2017) 6040–6046. doi:10.1021/acs.nanolett.7b02357.

[3] X. Long, G. Li, Z. Wang, H. Zhu, T. Zhang, S. Xiao, W. Guo, S. Yang, Metallic Iron-Nickel Sulfide Ultrathin Nanosheets As a Highly Active Electrocatalyst for Hydrogen Evolution Reaction in Acidic Media, J. Am. Chem. Soc. 137 (2015) 11900–11903. doi:10.1021/jacs.5b07728.

[4] L. Fan, P.F. Liu, X. Yan, L. Gu, Z.Z. Yang, H.G. Yang, S. Qiu, X. Yao, Atomically isolated nickel species anchored on graphitized carbon for efficient hydrogen evolution electrocatalysis, Nat. Commun. 7 (2016) 1–7. doi:10.1038/ncomms10667.

[5] J. Deng, P. Ren, D. Deng, L. Yu, F. Yang, X. Bao, Highly active and durable non-precious-metal catalysts encapsulated in carbon nanotubes for hydrogen evolution reaction, Energy Environ. Sci. 7 (2014) 1919–1923. doi:10.1039/C4EE00370E.

[6] J. Deng, P. Ren, D. Deng, X. Bao, Enhanced electron penetration through an ultrathin graphene layer for highly efficient catalysis of the hydrogen evolution reaction, Angew. Chemie - Int. Ed. 54 (2015) 2100–2104. doi:10.1002/anie.201409524.

[7] M. Tavakkoli, T. Kallio, O. Reynaud, A.G. Nasibulin, C. Johans, J. Sainio, H. Jiang, E.I. Kauppinen, K. Laasonen, Single-Shell Carbon-Encapsulated Iron Nanoparticles: Synthesis and High Electrocatalytic Activity for Hydrogen Evolution Reaction, Angew. Chemie. 127 (2015) 4618–4621. doi:10.1002/ange.201411450.

[8] Y. Shen, Y. Zhou, D. Wang, X. Wu, J. Li, J. Xi, Nickel–Copper Alloy Encapsulated in Graphitic Carbon Shells as Electrocatalysts for Hydrogen

Evolution Reaction, Adv. Energy Mater. 8 (2018) 1–7. doi:10.1002/aenm.201701759.

[9] K. Artyushkova, S. Pylypenko, M. Dowlapalli, P. Atanassov, Structure-to-property relationships in fuel cell catalyst supports : Correlation of surface chemistry and morphology with oxidation resistance of carbon blacks, J. Power Sources. 214 (2012) 303–313. doi:10.1016/j.jpowsour.2012.04.095.

[10] Y. Yang, Z. Lun, G. Xia, F. Zheng, M. He, Q. Chen, Non-precious alloy encapsulated in nitrogen-doped graphene layers derived from MOFs as an active and durable hydrogen evolution reaction catalyst, Energy Environ. Sci. 8 (2015) 3563–3571. doi:10.1039/C5EE02460A.

[11] S. Taubert, K. Laasonen, The molecular and magnetic structure of carbon-enclosed and partially covered Fe-55 particles, Phys. Chem. Chem. Phys. 16 (2014) 3648–3660. doi:10.1039/c3cp54491e.

[12] Y. Peng, S. Chen, Electrocatalysts based on metal@carbon core@shell nanocomposites: An overview, Green Energy Environ. 3 (2018) 335–351. doi:10.1016/j.gee.2018.07.006.

[13] F. Davodi, E. Mühlhausen, M. Tavakkoli, J. Sainio, H. Jiang, B. Gökce, G. Marzun, T. Kallio, Catalyst Support Effect on the Activity and Durability of Magnetic Nanoparticles: Toward Design of Advanced Electrocatalyst for Full Water Splitting, ACS Appl. Mater. Interfaces. 10 (2018) 31300–31311. doi:10.1021/acsami.8b08830.

[14] G. Marzun, A. Levish, V. Mackert, T. Kallio, S. Barcikowski, P. Wagener, Laser synthesis, structure and chemical properties of colloidal nickel-molybdenum nanoparticles for the substitution of noble metals in heterogeneous catalysis, J.

Colloid Interface Sci. 489 (2017) 57–67. doi:10.1016/j.jcis.2016.09.014.

[15] G. Marzun, H. Bönnemann, C. Lehmann, B. Spliethoff, C. Weidenthaler, S. Barcikowski, Role of Dissolved and Molecular Oxygen on Cu and PtCu Alloy Particle Structure during Laser Ablation Synthesis in Liquids, ChemPhysChem. 18 (2017) 1175–1184. doi:10.1002/cphc.201601315.

[16] H. Lawrence Clever, R. Battino, H. Miyamoto, Y. Yampolski, C.L. Young, IUPAC-NIST Solubility Data Series. 103. Oxygen and Ozone in Water, Aqueous Solutions, and Organic Liquids (Supplement to Solubility Data Series Volume 7), J. Phys. Chem. Ref. Data. 43 (2014) 033102.

[17] A. De Bonis, T. Lovaglio, A. Galasso, A. Santagata, Iron and iron oxide nanoparticles obtained by ultra-short laser ablation in liquid, Appl. Surf. 353 (2015) 433–438. http://www.sciencedirect.com/science/article/pii/S0169433215014920.

[18] Y.I. and K.S.D.Z. D. Zhang , W. Choi , Y. Oshima , U. Wiedwald, S. Cho , H. Lin, Y. Kuen Li, Magnetic Fe@FeOx, Fe@C and α-Fe2O3 Single-Crystal.pdf, Nanomaterials. 8 (2018) 631. doi:doi:10.3390/nano808063.

[19] J. Zhang, D.N. Oko, S. Garbarino, R. Imbeault, M. Chaker, A.C. Tavares, D. Guay, D. Ma, Preparation of PtAu alloy colloids by laser ablation in solution and their characterization, J. Phys. Chem. C. 116 (2012) 13413–13420. doi:10.1021/jp302485g.

[20] G. Cristoforetti, E. Pitzalis, R. Spiniello, R. Ishak, F. Giammanco, M. Muniz-Miranda, S. Caporali, Physico-chemical properties of Pd nanoparticles produced by Pulsed Laser Ablation in different organic solvents, Appl. Surf. Sci. 258 (2012) 3289–3297. doi:10.1016/j.apsusc.2011.11.084.

[21] A. Kanitz, J.S. Hoppius, M. del Mar Sanz, M. Maicas, A. Ostendorf, E.L. Gurevich, Synthesis of Magnetic Nanoparticles by Ultrashort Pulsed Laser Ablation of Iron in Different Liquids, ChemPhysChem. 18 (2017) 1155–1164. doi:10.1002/cphc.201601252.

[22] D. Zhang, B. Gökce, S. Barcikowski, Laser Synthesis and Processing of Colloids: Fundamentals and Applications, Chem. Rev. 117 (2017) 3990–4103. doi:10.1021/acs.chemrev.6b00468.

[23] V. Amendola, M. Meneghetti, What controls the composition and the structure of nanomaterials generated by laser ablation in liquid solution?, Phys. Chem. Chem. Phys. 15 (2013) 3027–3046. doi:10.1039/c2cp42895d.

[24] D.-H. Kim, M.-K. Paek, T.-J. Kim, S.-Y. Won, J.-J. Pak, Carbon Solubility in Liquid Iron Containing V, Mo and Ni, Mater. Trans. 55 (2014) 610–615. doi:10.2320/matertrans.M2013392.

[25] H. Yu, X. Li, X. Zeng, Y. Lu, Preparation of carbon dots by non-focusing pulsed laser irradiation in toluene, Chem. Commun. 52 (2016) 819–822. doi:10.1039/c5cc08384b.

[26] A. Kanitz, J.S. Hoppius, M. Fiebrandt, P. Awakowicz, C. Esen, A. Ostendorf, E.L. Gurevich, Impact of liquid environment on femtosecond laser ablation, Appl. Phys. A Mater. Sci. Process. 123 (2017) 1–7. doi:10.1007/s00339-017-1280-z.

[27] V. Amendola, P. Riello, M. Meneghetti, Magnetic nanoparticles of iron carbide, iron oxide, iron@iron oxide, and metal iron synthesized by laser ablation in organic solvents, J. Phys. Chem. C. 115 (2011) 5140–5146. doi:10.1021/jp109371m.

[28] N. Lasemi, U. Pacher, C. Rentenberger, O. Bomatí-Miguel, W. Kautek, Laser-Assisted Synthesis of Colloidal Ni/NiOxCore/Shell Nanoparticles in Water and Alcoholic Solvents, ChemPhysChem. 18 (2017) 1118–1124. doi:10.1002/cphc.201601181.

[29] D. Zhang, C. Zhang, J. Liu, Q. Chen, X. Zhu, C. Liang, Carbon-Encapsulated Metal/Metal Carbide/Metal Oxide Core–Shell Nanostructures Generated by Laser Ablation of Metals in Organic Solvents, ACS Appl. Nano Mater. 2 (2019) 28–39. doi:10.1021/acsanm.8b01541.

[30] V. Amendola, M. Meneghetti, What controls the composition and the structure of nanomaterials generated by laser ablation in liquid solution?, Phys. Chem. Chem. Phys. 15 (2013) 3027–3046. doi:10.1039/c2cp42895d.

[31] P. Wagener, J. Jakobi, C. Rehbock, V. Sai, K. Chakravadhanula, Solvent-surface interactions control the phase structure in laser- generated iron-gold core-shell nanoparticles, Sci. Rep. (2016) 1–12. doi:10.1038/srep23352.

[32] K. Matsumoto, Y. Okamoto, T. Nohira, R. Hagiwara, Thermal and Transport Properties of Na[N(SO 2 F) 2] − [N - Methyl - N - propylpyrrolidinium][N(SO 2 F) 2] Ionic Liquids for Na Secondary Batteries, Phys. Chem. C. 19 (2015) 7648−7655. doi:10.1021/acs.jpcc.5b01373.

[33] and M.E.M. K. L. McNerny, Y. Kim, D. E. Laughlin, McNerny et al. - 2010 - Chemical synthesis of monodisperse γ-Fe–Ni magnetic nanoparticles with tunable Curie temperatures for self-regul.pdf, J. Appl. Phys. (2010) 09A312. doi:doi:10.1063/1.3348738.

[34] R.T. Foley, Oxidation of Iron-Nickel Alloys, J. Electrochem. Soc. 109 (1962) 1202–1206.

[35] X.Z. D. Zhang, C. Zhang, J. Liu, Q. Chen, Carbon-Encapsulated Metal-Metal Carbide- Metal Oxide Core−Shell.pdf, ACS Appl. Nano Mater. (2019) 28−39.

[36] M. Byshkin, M. Hou, Phase transformations and segregation in Fe-Ni alloys and nanoalloys, J. Mater. Sci. 47 (2012) 5784–5793. doi:10.1007/s10853-012-6475-2.

[37] H. Zhang, C. Liang, J. Liu, Z. Tian, G. Shao, The formation of onion-like carbon-encapsulated cobalt carbide core/shell nanoparticles by the laser ablation of metallic cobalt in acetone, Carbon N. Y. 55 (2013) 108–115. doi:10.1016/j.carbon.2012.12.015.

[38] J. Rodríguez-Carvajal, Recent advances in magnetic structure determination by neutron powder diffraction, Phys. B Phys. Condens. Matter. 192 (1993) 55–69. doi:10.1016/0921-4526(93)90108-I.

[39] Y. Goto, K. Taniguchi, T. Omata, S. Otsuka-Yao-Matsuo, N. Ohashi, S. Ueda, H. Yoshikawa, Y. Yamashita, H. Oohashi, K. Kobayashi, Formation of Ni3C nanocrystals by thermolysis of nickel acetylacetonate in oleylamine: Characterization using hard X-ray photoelectron spectroscopy, Chem. Mater. 20 (2008) 4156–4160. doi:10.1021/cm703644x.

[40] M. Gong, H. Dai, A mini review of NiFe-based materials as highly active oxygen evolution reaction electrocatalysts, 8 (2015) 23–39. doi:10.1007/s12274-014-0591-z.

[41] A. Furlan, L. Hultman, M. Magnuson, Structure and bonding in amorphous iron carbide thin films, (2015). doi:10.1088/0953-8984/27/4/045002.

[42] E. Article, Z. Yang, T. Zhao, X. Huang, X. Chu, T. Tang, Y. Ju, Chemical

Science Modulating the phases of iron carbide nanoparticles : from a perspective of interfering with the carbon penetration of Fe @ Fe 3 O 4 by selectively adsorbed halide ions †, (2017) 473–481. doi:10.1039/c6sc01819j.

[43] T. Ma, M. Yuan, S.M. Islam, H. Li, S. Ma, G. Sun, X. Yang, FeNi3 alloy nanocrystals grown on graphene: Controllable synthesis, in-depth characterization and enhanced electromagnetic performance, J. Alloys Compd. 678 (2016) 468–477. doi:10.1016/j.jallcom.2016.03.243.

[44] M. Yuan, C. Nan, Y. Yang, G. Sun, H. Li, S. Ma, Uniform Fe x Ni y Nanospheres: Cost-Effective Electrocatalysts for Nonaqueous Rechargeable Li-O 2 Batteries, ACS Omega. 2 (2017) 4269–4277. doi:10.1021/acsomega.7b00497.

[45] D.L.A. de Faria, F.N. Lopes, Heated goethite and natural hematite: Can Raman spectroscopy be used to differentiate them?, Vib. Spectrosc. 45 (2007) 117–121. doi:10.1016/j.vibspec.2007.07.003.

[46] T. Sharifi, E. Gracia-Espino, H. Reza Barzegar, X. Jia, F. Nitze, G. Hu, P. Nordblad, C.W. Tai, T. Wagberg, Formation of nitrogen-doped graphene nanoscrolls by adsorption of magnetic gamma-Fe2O3 nanoparticles, Nat Commun. 4 (2013) 2319. doi:10.1038/ncomms3319.

[47] A.M. Jubb, H.C. Allen, Vibrational spectroscopic characterization of hematite, maghemite, and magnetite thin films produced by vapor deposition, ACS Appl. Mater. Interfaces. 2 (2010) 2804–2812. doi:10.1021/am1004943.

[48] Y. Yeh, H.M. Chen, R. Liu, K. Asakura, M. Lo, Y. Peng, T. Chan, J. Lee, Pd - C - Fe Nanoparticles Investigated by X-ray Absorption Spectroscopy as Electrocatalysts for Oxygen Reduction, Chem. Mater. (2009) 4030–4036.

doi:10.1021/cm901383x.

[49] L. Du, L. Luo, Z. Feng, M. Engelhard, X. Xie, B. Han, J. Sun, J. Zhang, G. Yin, C. Wang, Y. Wang, Y. Shao, Nitrogen–doped graphitized carbon shell encapsulated NiFe nanoparticles: A highly durable oxygen evolution catalyst, Nano Energy. 39 (2017) 245–252. doi:10.1016/j.nanoen.2017.07.006.

[50] L. Du, L. Luo, Z. Feng, M. Engelhard, X. Xie, B. Han, Nano Energy Nitrogen – doped graphitized carbon shell encapsulated NiFe nanoparticles : A highly durable oxygen evolution catalyst, Nano Energy. 39 (2017) 245–252. doi:10.1016/j.nanoen.2017.07.006.

[51] A.G. Osorio, C.P. Bergmann, Evaluation of iron-containing carbon nanotubes by near edge X-ray absorption technique, Radiat. Phys. Chem. 115 (2015) 164–170. doi:10.1016/j.radphyschem.2015.07.001.

[52] S. Uhlig, R. Struis, H. Schmid-engel, J. Bock, A. Probst, O. Freitag-weber, I. Zizak, R. Chernikov, G. Schultes, Diamond & Related Materials Piezoresistive Ni : a-C : H thin fi lms containing hcp-Ni or Ni 3 C investigated by XRD , EXAFS , and wavelet analysis, Diam. Relat. Mater. 34 (2013) 25–35. doi:10.1016/j.diamond.2013.01.013.

[53] B. Alsabban, L. Falivene, S.M. Kozlov, A. Aguilar-tapia, S. Ould-chikh, J. Hazemann, L. Cavallo, J. Basset, K. Takanabe, Applied Catalysis B : Environmental In-operando elucidation of bimetallic CoNi nanoparticles during high-temperature CH 4 / CO 2 reaction, "Applied Catal. B, Environ. 213 (2017) 177–189. doi:10.1016/j.apcatb.2017.04.076.

[54] R.P.W.J. Struis, D. Bachelin, C. Ludwig, A. Wokaun, Studying the Formation of Ni 3 C from CO and Metallic Ni at T) 265 ° C in Situ Using Ni K-Edge X-ray

Absorption Spectroscopy, (2009) 2443–2451.

[55] K. Asakura, Experimental Database XAFS as an example, 2018. doi:10.1107/S1600577518006963.Introduction.

[56] Massalski T.B., Binary Alloy Phase Diagrams, vol. 1 (2nd Edit.), Metals Park, Ohio, 2001. http://www.isbnsearch.org/isbn/978-0-87170-403-0.

[57] D.J. Steinberg, A Simple Relationship Between the Temperature Dependence of the Density of Liquid Metals and Their Boiling Temperatures, Metall. Trans. 5 (1974) 1341–1343.

[58] Z. Yan, D.B. Chrisey, Journal of Photochemistry and Photobiology C : Photochemistry Reviews Pulsed laser ablation in liquid for micro- / nanostructure generation, "Journal Photochem. Photobiol. C Photochem. Rev. 13 (2012) 204–223. doi:10.1016/j.jphotochemrev.2012.04.004.

[59] C. Zhang, and T.Y. M. Hou , J. Lin , Y. Liu, S. Feng, C. Jin, Electrical Resistivity of Fe-C Alloy at High Pressur Effects of Carbon as a Light Element on the Thermal Conductivity of the Earth's Core, J. Geophys. Res. Solid Earth Res. (2018) 3564. doi:10.1029/2017JB015260.

[60] E. Zoulias, E. Varkaraki, A review on water electrolysis, 2004. http://large.stanford.edu/courses/2012/ph240/jorna1/docs/zoulias.pdf.

[61] J. Kibsgaard, T.F. Jaramillo, F. Besenbacher, Building an appropriate active-site motif into a hydrogen-evolution catalyst with thiomolybdate [Mo3S13]2- clusters, Nat. Chem. 6 (2014) 248–253. doi:10.1038/nchem.1853.

[62] W.F. Chen, C.H. Wang, K. Sasaki, N. Marinkovic, W. Xu, J.T. Muckerman, Y. Zhu, R.R. Adzic, Highly active and durable nanostructured molybdenum

carbide electrocatalysts for hydrogen production, Energy Environ. Sci. 6 (2013) 943–951. doi:10.1039/c2ee23891h.

[63] B.E. Conway, B. V Tilak, Interfacial processes involving electrocatalytic evolution and.pdf, 47 (2002). doi:10.1016/S0013-4686(02)00329-8.